Investigating Spatial and Temporal Structuring of E-Region Coherent Scattering Regions Over Northern Norway

Devin Huyghebaert[1] , Jorge L. Chau[2] , Andres Spicher[1] , Magnus F. Ivarsen[3,4] , Matthias Clahsen[2] , Ralph Latteck[2] , and Juha Vierinen[1]

[1]Department of Physics and Technology, UiT The Arctic University of Norway, Tromsø, Norway, [2]Leibniz Institute of Atmospheric Physics at the University of Rostock, Kühlungsborn, Germany, [3]Department of Physics and Engineering Physics, University of Saskatchewan, Saskatoon, SK, Canada, [4]Department of Physics, University of Oslo, Oslo, Norway

Abstract Recently, it has been shown that the Spread Spectrum Interferometric Multistatic meteor radar Observing Network radar system located in northern Norway is capable of measuring ionospheric E-region coherent scatter with spatial and temporal resolutions on the order of 1.5 km and 2 s, respectively. Four different events from June and July of 2022 are examined in the present study, where the coherent scatter measurements are used as a tracer for large-scale ionospheric phenomena such as plasma density enhancements and ionospheric electric fields. By applying a two-dimensional Fourier analysis to range-time-intensity data, we perform a multi-scale spatial and temporal investigation to determine the change in range over time of large-scale ionospheric structures (>3 km) which are compared with line-of-sight velocities of the small scale structures (∼5 m) determined from the Doppler shift of the coherent scatter. The spectral characteristics of the large-scale structures are also investigated and logarithmic spectral slopes for scale sizes of 100–10 km were found to be between −3.0 and −1.5. This agrees with much of the previous work on the spatial spectra scaling for ionospheric electric fields. This analysis aids in characterizing the source of the plasma turbulence and provides crucial information about how energy is redistributed from large to small scales in the E-region ionosphere.

Plain Language Summary Large electromagnetic structures and processes at scales greater than 1 km influence the ionosphere of the Earth. Coherent scatter ionospheric radars measure meter-scale plasma turbulence that can be caused by these structures. This small-scale turbulence in the E-region (90–150 km altitude) is related to the electric fields and plasma density of the ionosphere. In this study, we use the coherent scatter measurements as a tracer for the large-scale processes occurring. By examining the structure of the small-scale turbulence within a large field of view, we can then look at the physics behind the large-scale structures and how they drive the small-scale turbulence. We can also investigate the cascade of energy between the different scales in turbulent regions.

1. Introduction

Kolmogorov, in 1941, discussed the cascade of kinetic energy from large-scale eddies to smaller-scale eddies within high Reynolds number isotropic fluid turbulence (Kolmogorov et al., 1991). The expected slope when the power spectrum of the data was plotted on a logarithmic scale was found to be −5/3, which has been used abundantly as a comparison value in a wide range of turbulence studies. This slope is what is considered to be in the "inertial" range of scale sizes. At scale sizes below this, a steepening of the slope is expected, which has been termed the dissipative, or dissipation, region (e.g., Debue et al., 2018). We already know from the process of ionospheric coherent scattering that ionospheric plasma turbulence is not isotropic, where the largest power of fluctuations in the plasma irregularity spectrum commonly lie perpendicular to the geomagnetic field. Nonetheless, the Kolmogorov study does provide a baseline for investigating the spectral slopes of the ionospheric turbulence data and has been cited and considered by previous ionospheric turbulence researchers (e.g., Kintner & Seyler, 1985).

Studies on the power decay of turbulence have been extended to the ionosphere using various different instruments (e.g., Chaston et al., 2011; Ivarsen et al., 2021; Kintner & Seyler, 1985; Kozelov & Rypdal, 2007; Ott & Farley, 1974; Pécseli, 2015; Spicher et al., 2014). The slopes of the spectra show varying levels of agreement with the −5/3 predicted by Kolmogorov, where the disagreements have commonly been attributed to different ionospheric phenomena, such as plasma instabilities. Some of the devices used in these studies include auroral

imagers, satellite instruments, and rocket instruments. The measurement quantities that have been focused on previously include the plasma density, the ionospheric electric potential, the ionospheric electric field, and fluctuations in magnetic field measurements.

In the present study, we measure coherent scatter from E-region small-scale turbulence (<10 m) to determine the structuring of the ionosphere on relatively large scales (>3 km). The majority of this scatter is considered to be perpendicular to the geomagnetic field, both at E-region and F-region altitudes. At E-region altitudes in the auroral regions, the meter-scale turbulence is typically caused by the Farley-Buneman, or two-stream, plasma instability (Buneman, 1963; Farley, 1963) and the gradient drift instability (Fejer & Kelley, 1980). Both of these instabilities are affected by the electric field strength and direction in the E-region ionosphere. For further reviews on the formation and characteristics of E-region plasma instabilities measured with coherent scatter radars, the reader is referred to Hysell (2015) and Chau and St.-Maurice (2016), and the references therein.

Using radars for spatial and temporal correlations and measurements of structuring is not novel. For example, a recent study using second-order statistics of line-of-sight velocities investigated the spatial and temporal correlations of horizontal neutral atmospheric winds in the mesosphere and lower thermosphere (Vierinen et al., 2019). In the study, the temporal and spatial resolutions obtained were dependent on the occurrence and spacing of meteor trail measurements, where 10^5 independent meteor trails could be observed in 24 hr. For E-region coherent scatter during active ionospheric periods, it is possible to obtain a similar number of measurements in 10 min, where the measurements are commonly grouped in time and space. The recent studies of Ivarsen, St-Maurice, et al. (2023) and Ivarsen, Lozinsky, et al. (2023) highlight the clustering of ionospheric E-region scatter. This clustering of measurements provides an opportunity to measure the lower thermosphere ionospheric turbulence structuring in relatively fine temporal and spatial resolution.

Extended spectral analyses of ionospheric coherent scatter measurements to investigate large-scale structures have been possible with previous radar systems—imaging and/or wave analysis has been performed on SuperDARN data (e.g., Bristow, 2019; Shi et al., 2018), mid-latitude E-region coherent scatter (e.g., Hysell & Larsen, 2021), and auroral E-region coherent scatter (e.g., Hysell et al., 2012; Ivarsen, Lozinsky, et al., 2023). A modeled example of how signatures of magnetospheric sources would appear in Doppler radars is provided in Archer et al. (2023), showing the possibility of waves with periodicities on the order of 600 s being seen in the Doppler shift of radar measurements. Advances in the accuracy, resolution, and computing power available now allow us to perform spectral analysis on coherent scatter in multiple dimensions at relatively high resolutions.

We are able to obtain simultaneous km-scale and second-scale resolutions with radars over a greater than 10,000 km^2 field of view in the E-region. Using these relatively fine-scale resolutions, the large-scale ionospheric driving processes can now be further investigated. Some examples of recent auroral E-region coherent scatter radar studies utilizing imaging and/or high temporal and spatial resolutions include Hysell et al. (2012), Chau and St.-Maurice (2016), Huyghebaert et al. (2019), and Lozinsky et al. (2022). SuperDARN coherent scatter radars are also being upgraded for higher resolution modes with modern hardware (Bristow, 2019; McWilliams et al., 2023). It is expected that the analyses presented here could be applied to such radars.

The current study focuses on coherent scatter radar measurements in the northern auroral zone of Norway, where the Spread Spectrum Interferometric Multistatic meter radar Observing Network (SIMONe) Norway meteor radar system operates. We consider the E-region coherent scatter measurements to correspond to a combination of the ionospheric electric field (plasma density irregularity generation) and the bulk plasma density (scattering cross-section/power) (e.g., Huyghebaert et al., 2021), and use the small-scale plasma turbulence measurements as a tracer for the larger scale drivers of the turbulence on km and greater scales (e.g., Hysell & Larsen, 2021; Ivarsen, Lozinsky, et al., 2023). It has already been shown previously that the SIMONe meteor radar system is capable of measuring different auroral ionospheric phenomena including E-region coherent scatter, in addition to its main purpose of measuring neutral winds in the upper mesosphere (Chau et al., 2019; Huyghebaert et al., 2022).

2. Instrument and Methodology

The SIMONe Norway meteor radar system was first installed in 2021 and since then has been expanded to include eight different radar links operating at 32.55 MHz in the Fennoscandia sector. The system was developed and deployed to investigate mesospheric winds at auroral latitudes, with the goal to further understand the solar-terrestrial coupling of the charged and neutral atmospheres. One of the features of the system is the

software-defined radio design, allowing multiple different signal processing algorithms to be implemented in the analysis of the radar signal. We take advantage of this to investigate the plasma existing in the E-region ionosphere.

Using the SIMONe radar system for E-region coherent scatter has been described previously by Huyghebaert et al. (2022). As a summary, the complex voltage values of the received signal can be recorded by the SIMONe Norway systems. The recorded complex voltage data were processed using similar techniques as the ICEBEAR system in Canada (Huyghebaert et al., 2019). Due to the coherent multi-input-single-output and coding used by the SIMONe Norway system, a self-interference (self-clutter) reduction algorithm was implemented in the analysis.

From the range-Doppler-Intensity measurements, a Gaussian curve was fit to the spectra for each range with valid data and mapped to the SIMONe Norway field of view. This provided multiple details about the signal, including the SNR, spectral width, Doppler shift, range, and angle of arrival. The interferometry for the spread targets was found to be reliable on a statistical basis and less reliable for single points of data. For this reason, the current study only considers the average azimuth and altitude of the E-region coherent scatter when using the interferometry location data. The range-time-intensity data, along with the associated spectral width, are used for the majority of the analysis.

The data collected for this analysis had the transmitter code lengthened to 200 ms (20,000 pseudo-random binary bits) from 10 ms (1,000 pseudo-random binary bits). This provided improved self-clutter suppression in the analysis of the signal. This was a temporary test implementation, though there are plans to further integrate the longer code into the common operations analysis procedure. For neutral wind estimations, the SIMONe system has been using the shorter codes (10 ms) (e.g., Chau et al., 2021; Huyghebaert et al., 2022).

To illustrate the data processing chain implemented for this study, a block diagram is provided in Figure 1. This provides a summary of what processing was performed to create each of the figures displaying the radar data. Note that this block diagram provides a summary of the processing, with the finer details of the processing being provided in the text.

Four different active ionospheric events during June and July of 2022 were recorded and processed. The close to monostatic link of Andenes-Saura records the most data and is therefore focused on. The authors believe the reason for this link recording the most data is due to significant refraction of the signal being required for measurements to be made perpendicular to the geomagnetic field. If the bisector angle for scatter is large, potentially two locations with large plasma densities are required for an optimal scattering signal path for receiving the signal. With a close to monostatic setup, only one relatively localized region of large electron density is required.

The integrated SNR, Doppler velocity, and the azimuth of the E-region coherent scatter are provided in Figure 2 for the dates analyzed. Data with a Doppler shift within the bounds of ±100 m/s with a spectral width less than 50 m/s were filtered from the data. Data with a total propagation distance less than 250 km were also filtered. These filters were implemented to reduce the measurements of groundscatter and meteor echoes included in the analysis.

The integrated SNR refers to the standard deviation of the Gaussian fitted to the spectra for a given range multiplied by the peak SNR of the range. This provides an estimate of the integrated small-scale plasma turbulence occurring for a given range in the radar field of view. The bistatic Doppler velocity is not corrected since the effect is expected to be minimal due to the close to monostatic setup of the Andenes-Saura bistatic radar link. The interferometry analysis also included occasional errors in the angle of arrival determination which contributed to the decision to use monostatic range and Doppler shift values. The total signal propagation distance is therefore divided by 2 for the approximate range to the radar system, with a resulting spatial resolution of 1.5 km.

Due to the positive and negative Doppler velocities of E-region coherent scatter originating from different locations in the system field of view, these were separated when performing the further analyses if a time period had a significant number of positive and negative Doppler shifts. This can be seen for the events on 27 July 2022 shown in the bottom panels of Figure 2.

We focus on the range-time-integrated SNR data, which are the top panels for each of the events in Figure 2. A two-dimensional (2D) Fast Fourier Transform (FFT) analysis is performed on the data, after any nonexistent integrated SNR values are assigned a value of 15 and after subtracting the mean of the data. Setting the lowest integrated SNR value to 15 dB is to reduce artifacts in the 2D FFT analysis, and is the approximate lower cutoff of
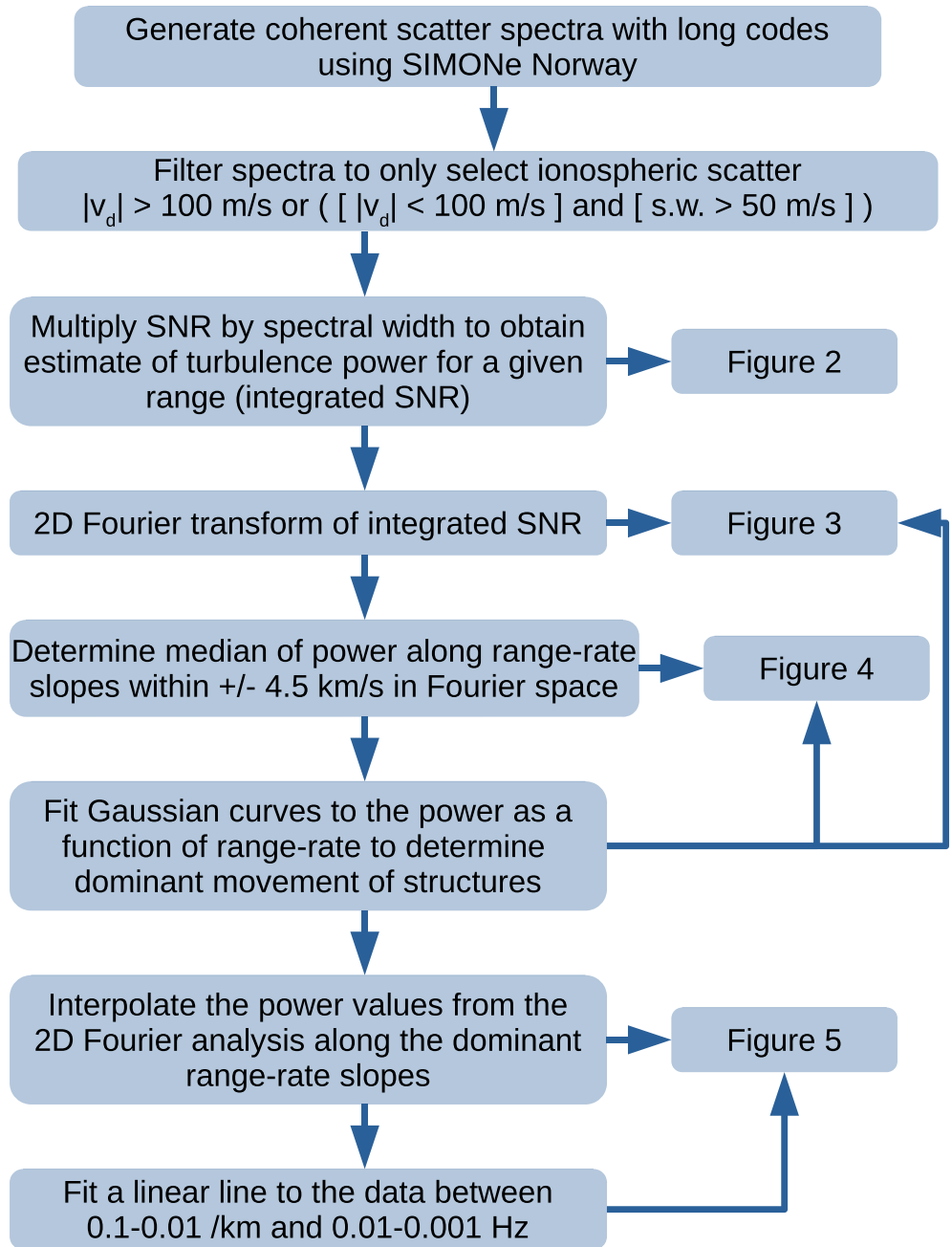
Generate coherent scatter spectra with long codes using SIMONe Norway

↓

Filter spectra to only select ionospheric scatter
$|v_d| > 100$ m/s or ([$|v_d| < 100$ m/s] and [s.w. > 50 m/s])

↓

Multiply SNR by spectral width to obtain estimate of turbulence power for a given range (integrated SNR) → Figure 2

↓

2D Fourier transform of integrated SNR → Figure 3

↓

Determine median of power along range-rate slopes within +/- 4.5 km/s in Fourier space → Figure 4

↓

Fit Gaussian curves to the power as a function of range-rate to determine dominant movement of structures

↓

Interpolate the power values from the 2D Fourier analysis along the dominant range-rate slopes → Figure 5

↓

Fit a linear line to the data between 0.1-0.01 /km and 0.01-0.001 Hz

Figure 1. Block diagram of the data processing workflow to obtain the results presented in this study. Further descriptions of each of the processing blocks are provided in the text. v_d refers to the Doppler velocity, and *s.w.* refers to the spectral width.

the integrated SNR data. This Fourier analysis can provide details about the structuring of the ionospheric coherent scatter, and therefore plasma turbulence, as a function of both space and time for different scale sizes. We can also investigate the bulk motion of the ionospheric plasma based on the values along slopes in the 2D Fourier space (velocities, or hereafter defined as range-rates) corresponding to the largest integrated spectral powers. The range-rate refers to the change in range over time of ionospheric structures with respect to the radar location. The results from the 2D FFT analysis are presented in Figure 3.

In Figure 3, it is clear that the power of the 2D FFT is concentrated at certain slope values, corresponding to certain range-rates for the SIMONe system. To determine the slopes with the greatest integrated power, a further fitting analysis is performed.
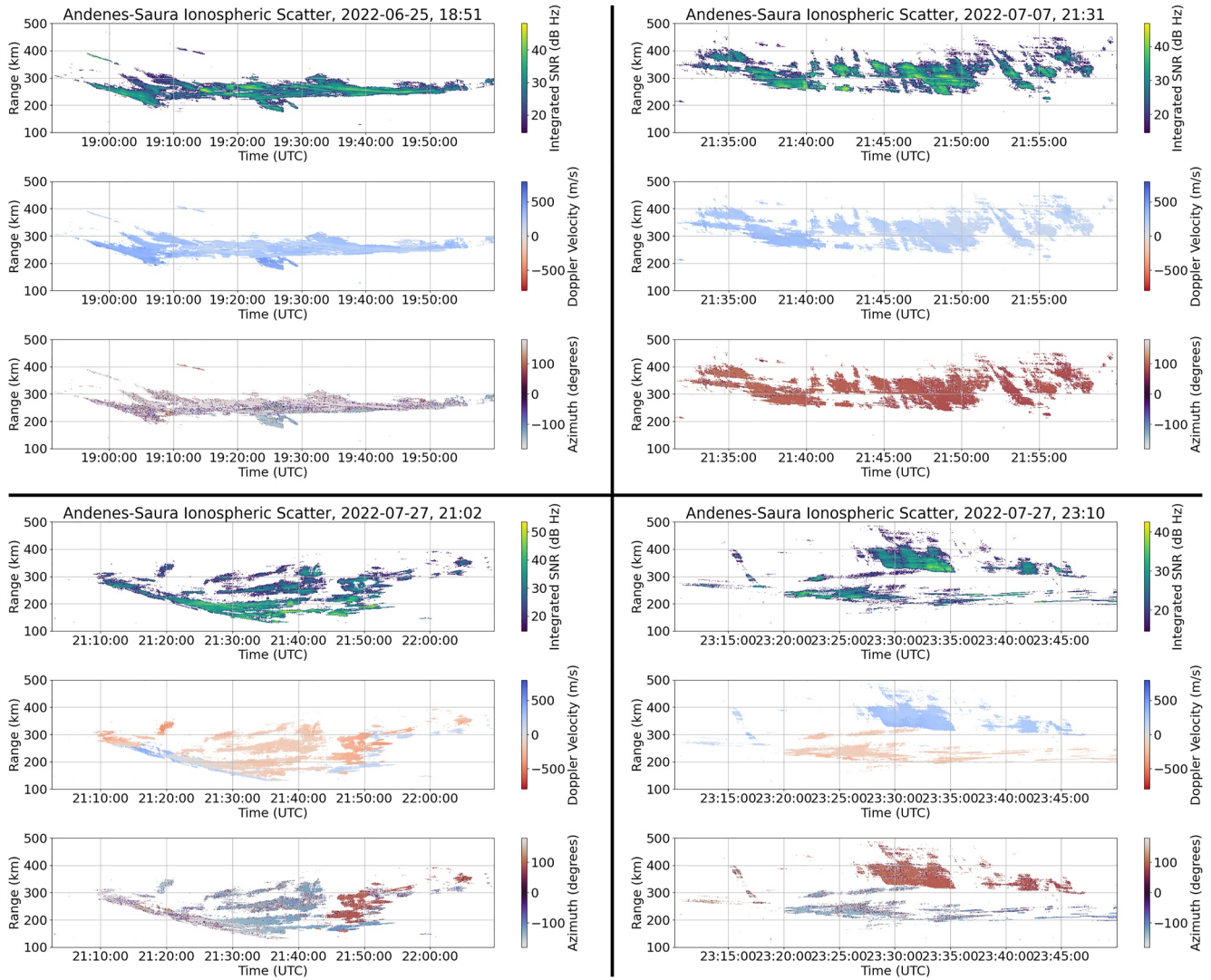
Figure 2. Summary plots of the events analyzed in the present study. The integrated SNR is calculated by multiplying the SNR by the standard deviation of the Gaussian that was fit to the spectra for a given range thereby providing a measure of the spectral width. The integrated SNR is then converted to a logarithmic scale.

Power values along a line corresponding to a range-rate slope passing through the origin of the 2D Fourier analyzed data are determined after a one-sigma (one array element standard deviation along each axis) Gaussian smoothing filter is applied on the 2D array. A correction to the magnitude is applied to account for the distance from the origin of each of the points. The maximum values of the axes are used to scale the results. Therefore, points that are further from the origin have their magnitude increased more than those closer. This was done to reduce the influence of only the largest scales when determining the dominant range-rates in the data. Note that this is only applied to the data in Figure 4 for determining the range-rates of the ionospheric structures. The median of the interpolated values is used to provide a single value for the power for a given slope (range-rate). Velocities between −4.5 and 4.5 km/s in 5 m/s increments (1,800 intervals) were considered in the analysis, though only the data between −2.0 and 2.0 km/s are presented as no significant trends were found outside these range-rate values.

A spectral power to mean ratio (SPMR) is created, where the data is converted by the equation:

$$SPMR = \frac{SP - M}{M} \tag{1}$$

where SP is the spectral power of the signal as a function of the range-rate, which in this case is the median of the interpolated values along each range-rate slope, and M is the mean of the median spectral power data from
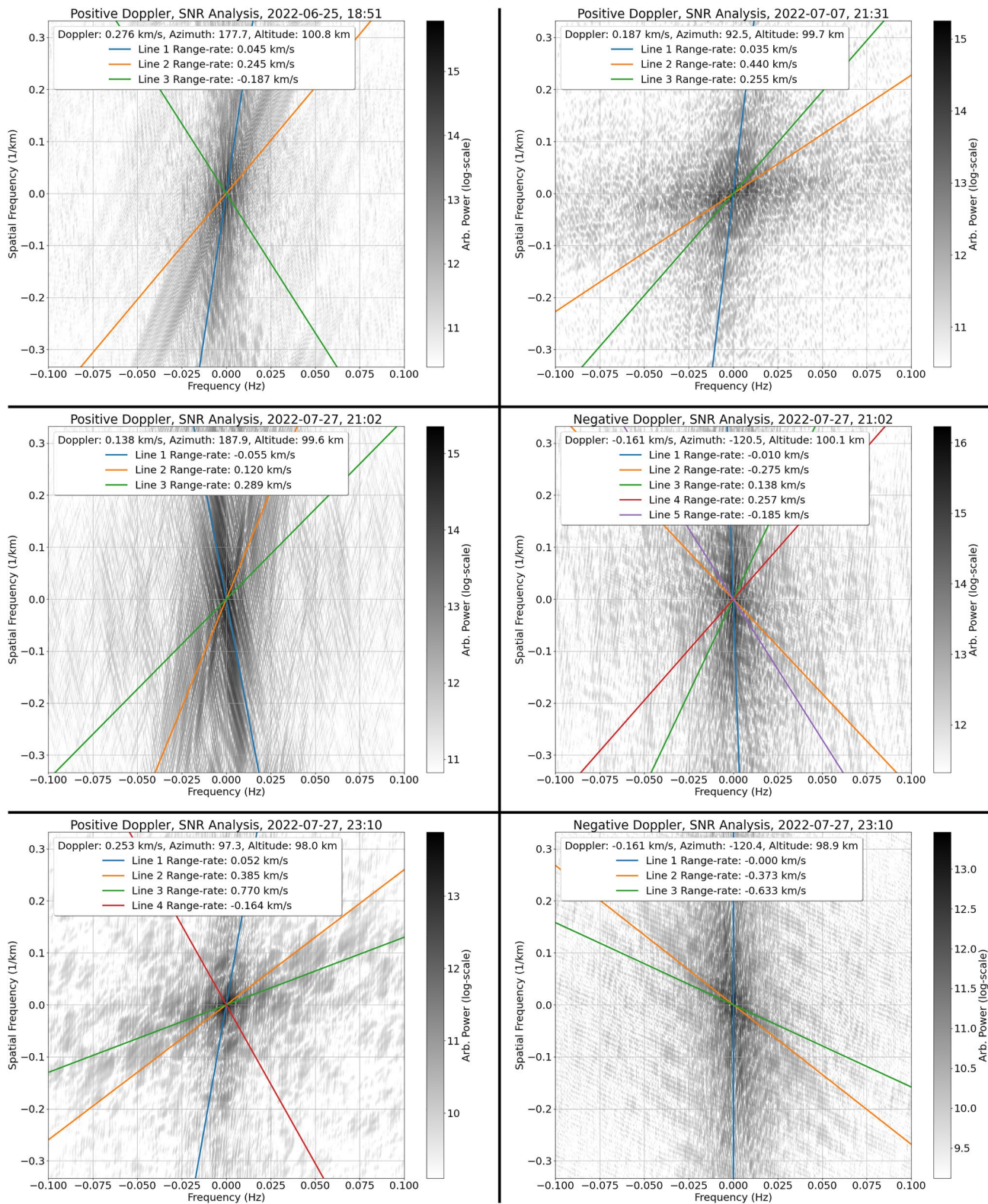
Figure 3. The 2D FFT analysis performed on the integrated SNR range-time-intensity data is shown in Figure 2. The positive and negative Doppler shifts have been separated into different analyses for the events on 27 July 2022. The legends in the figures list the median Doppler, azimuth, and altitude for the E-region coherent scatter during the full time period, as well as the range-rate values determined for the data (described further in text). The lines corresponding to the range-rate values are included in the figures.

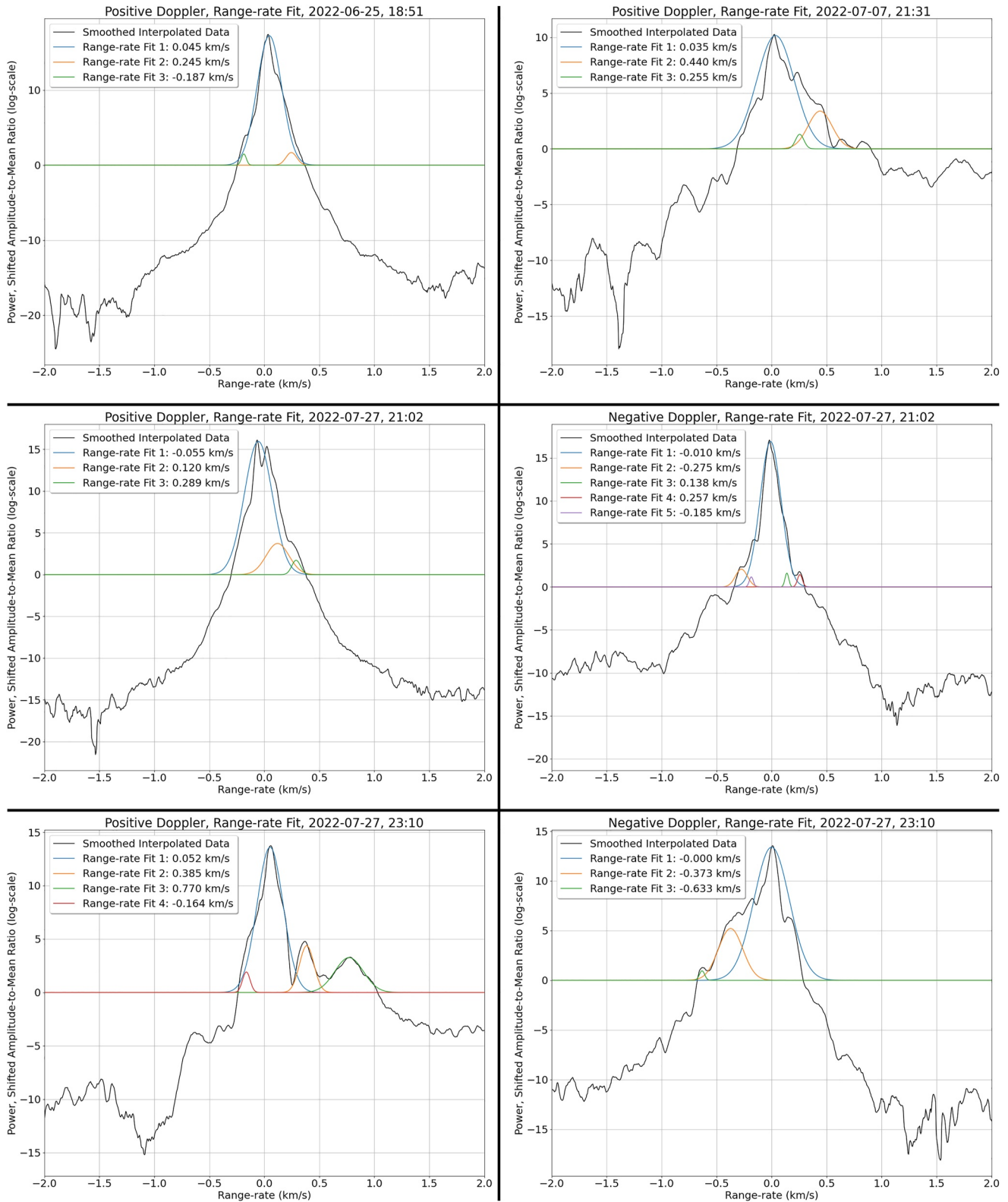**Figure 4.** Plots of the smoothed 2D FFT interpolated data and fitted Gaussian curves to the data to determine the dominant range-rates of the ionospheric plasma. This was derived from the data presented in Figure 3. The range-rates determined from this analysis are provided in the legend for each of the Gaussian fits. The filtering performed to the original data is described in the text.

±4.5 km/s. The data is then shifted by the minimum value of SPMR so that all values are above 0, and the results are converted to a log-scale. A 10-sample running average is then performed on the data. The results from this are presented in Figure 4, and are shown as the black traces in the panels.

To determine the dominant range-rates of the data, we consider only the data above a value of 0 dB. Gaussian curves are then fit to the data. Each Gaussian fit is subtracted from the data before the next curve is fit. A value of 0.8 dB is set as the threshold, where if no peaks are left above this value the fitting process stops. This algorithm provides the range-rates listed in the legends of Figures 3 and 4. These range-rates are then used to sample the temporal and spatial structuring space from the 2D FFT analysis to examine structures in the reference frame of the plasma motion.

Using the derived range-rates, the 2D Fourier analyzed data is interpolated and sampled along these slopes with the starting point at the origin. Along each of these lines, the spatial and temporal frequencies are considered separately. The results from this are presented in Figure 5. The power spectra as a function of the spatial frequency and temporal frequency are thereby provided in the reference frames of the range-rates given in the legends.

A linear regression line for the spectral power is fit for both temporal frequency and spatial frequency. The temporal frequency line is fit between frequencies of 0.001–0.01 Hz (1,000–100 s period), and the spatial frequency line is fit between frequencies of 0.01–0.1/km (100–10 km scales). These scales were selected in the data to represent relatively large-scale structures in both space and time. The linear regression lines are included in the figure, with the slope of each line provided in the legends.

The next section discusses and puts these results in the context of previous research on the topic. It should be noted that E-region studies involving the turbulence spectrum are relatively rare, with most analyses using rocket or satellite in-situ measurements and auroral imagers. It therefore needs to be highlighted that (a) these measurements were recorded in the summer at high latitudes and can be made in sunlit ionospheric conditions, and (b) the relatively large field of view of the radar provides a consistent sampling of the plasma turbulence over relatively long periods of time. This makes E-region coherent scatter unique in its ability to sample the ionosphere at an altitude of ~100 km over long periods of time at consistent resolutions within a large field of view during both sunlit and dark conditions.

3. Results and Discussion

Before discussing the values of the derived spectral slopes, the general characteristics of the data are first described and investigated. It is important to stress that we consider the small-scale turbulence field measured by SIMONe to be caused by larger-scale sources that structure both the ionospheric electric fields and E-region plasma density. We therefore are not investigating the small-scale properties of the plasma irregularities; rather, we investigate km scale structuring of the location and intensity of the turbulence in the radar field of view.

From Figure 4, the most power in the large-scale plasma structures occurs at approximately 0.0 km/s range-rate. This corresponds to turbulence commonly occurring at the same range over the course of the measurements. The peak is not necessarily at 0 km/s, which corresponds to slight movement of the particle precipitation regions, change of the electric fields, and/or neutral wind motion influencing the plasma turbulence for the range-rates observed. The measurement of E-region coherent scatter with SIMONe Norway is complicated, as we expect the signal to require both sufficient refraction to be perpendicular to the geomagnetic field (large plasma densities), and for there to be a sufficient radar scattering cross section of the plasma (sufficient plasma turbulence and plasma density) at the scattering location. This combination could be a driving factor in the range of the scatter being relatively consistent over most of the measurements. Previous research by Nakai et al. (1986) found time scales of 45 min for the expansion of the auroral oval and 8 hr for the contraction of the auroral oval. The relatively slowly varying locations of E-region plasma turbulence over time scales of approximately 1 hr are therefore not unexpected.

The determined range-rates of the large-scale plasma structures do not necessarily match the Doppler shift of the coherent scatter in the E-region plasma. The motion of the large-scale plasma structures corresponds to the ionospheric and/or magnetospheric source of the small-scale plasma turbulence. The diffusion rate of the plasma in the E-region is relatively high, so it is expected that magnetospheric processes are the source for sufficient electric fields and/or electron densities for both plasma instabilities to develop and for there to be sufficient radar scattering cross sections for measurements to be made.

The range-rates were found to be rarely above the assumed ion-acoustic speed of ~ 400 m/s. No plasma temperature data were available for this study and therefore the ion-acoustic speed is an estimate. The average Doppler shifts of the coherent scatter correspond to relatively slow E-region coherent scatter and we expect that there is significant refraction of the signal. SuperDARN has been known to under-estimate the ionospheric motion of the plasma in the F-region due to index of refraction effects (e.g., Gillies et al., 2009). There is potentially a similar effect occurring here, where significant amounts of refraction of the signal are required to become perpendicular to the magnetic field. Another factor that could be affecting the Doppler shifts of the coherent scatter is that the altitudes of the scatter are relatively low and the measurements may not be in the direction of the $E \times B$ ionospheric plasma motion. There have also been studies on the Modulated Electron Ohmic Heating by Waves mechanism to produce narrow, relatively slow E-region coherent scatter (St.-Maurice & Chau, 2016), which could correspond to the relatively slow Doppler shifts observed. In addition, a previous study by St.-Maurice et al. (1994) has suggested that plasma density gradients may be the cause of the coherent scatter measurements at less than the ion-acoustic speed. For the present study, we only consider that there is turbulence occurring in the measurement region which we attribute to enhanced electric fields and plasma densities.

If we further examine Figure 5, we can observe that the slopes of the spatial frequencies corresponding to scale sizes less than 10 km are more shallow than those at larger scales. This is opposite from what is expected in turbulence studies without some source of energy at the smaller scales. This could be the result of random small fluctuations in the radar SNR and/or spectral width measurements resulting in a noise-like signal with a constant value power spectrum. As well, the spatial scales of 10 km approach the Nyquist sampling threshold of 3 km and we are unable to extend the measurements to smaller than km scales. Even considering these factors, scales at less than 10 km can correspond to auroral arc sizes (Samson et al., 1996), and could be a source of structuring for the E-region plasma turbulence. A recent study by Ivarsen, Lozinsky, et al. (2023) has also shown the decrease in magnitude of slopes at ~ 10 km scales, where the decrease is clearly interpreted as an increase in small-scale power. In that study, matching spectral shapes were simultaneously seen in FAC structuring as measured in situ by a Swarm satellite, leading the authors to conclude that FAC structuring was driving the E-region tracer echoes. Future investigations with higher bandwidth transmit setups (higher range resolution) could investigate these turbulence scales in further detail using SIMONe.

For the temporal power spectra, we see an opposite trend. In four of the panels of Figure 5, the slope of the spectra in the temporal domain appears to become steeper at scales of 100–10 s. This could correspond to the auroral structuring occurring at timescales of 1,000–100 s rather than 100-10s for these measurements. The steepening of power spectra can also be interpreted as tell-tale signs of irregularity dissipation, which have been observed in the topside F-region plasma (Ivarsen et al., 2019; Kivanç & Heelis, 1998). This is not to say that there is no source of structuring at smaller temporal scales (higher frequencies), where we know from previous studies that there are commonly injections of power from, for example, Alfvén waves (Pakhotin et al., 2018). This is only to say that there could potentially be a lack of power injection into the ionosphere and/or a suppression of turbulence generation occurring at the intermediate temporal scales of 100–10s during some of these events, which could correspond to a lack of magnetospheric waves with periods on this order.

A previous study investigated SuperDARN data for magnetospheric waves and found there to be some latitude dependence on the frequency of waves observed. Pc4-5 wave frequencies were found at auroral/polar latitudes, while Pc3-4/Pi2 were found at mid-latitudes (Shi et al., 2018). Pc refers to pulsations continuous, while Pi refers to pulsations irregular, and the number following refers to the frequency of the magnetospheric wave classification. The occurrence of the magnetospheric waves was found to be lowest in the summer and only clear wave occurrences were investigated, rather than the broad spectral sources and cascading power we investigate with the current spectral slope analysis. There was a distinct lack of wave activity at frequencies of 20–40 mHz (25–50 s periods) in the Pc3-4/Pi2 analysis of their data. This lack of wave activity at 25–50 s scales is consistent with the observations in the present study of the steepening slopes of E-region data at 100–10 s scales, though the corresponding latitude of the results differ. The further analysis of magnetospheric wave signatures in SIMONe auroral E-region coherent scatter data is a research endeavor left for a future study.

A summary of the slopes from the different events is provided in Figure 6. The majority of positive Doppler-shifted data had positive range-rates, and negative Doppler-shifted data had negative range-rates. There were also occurrences of range-rates corresponding to opposite direction motion of the large-scale structures when compared with the small-scale turbulence Doppler shifts.
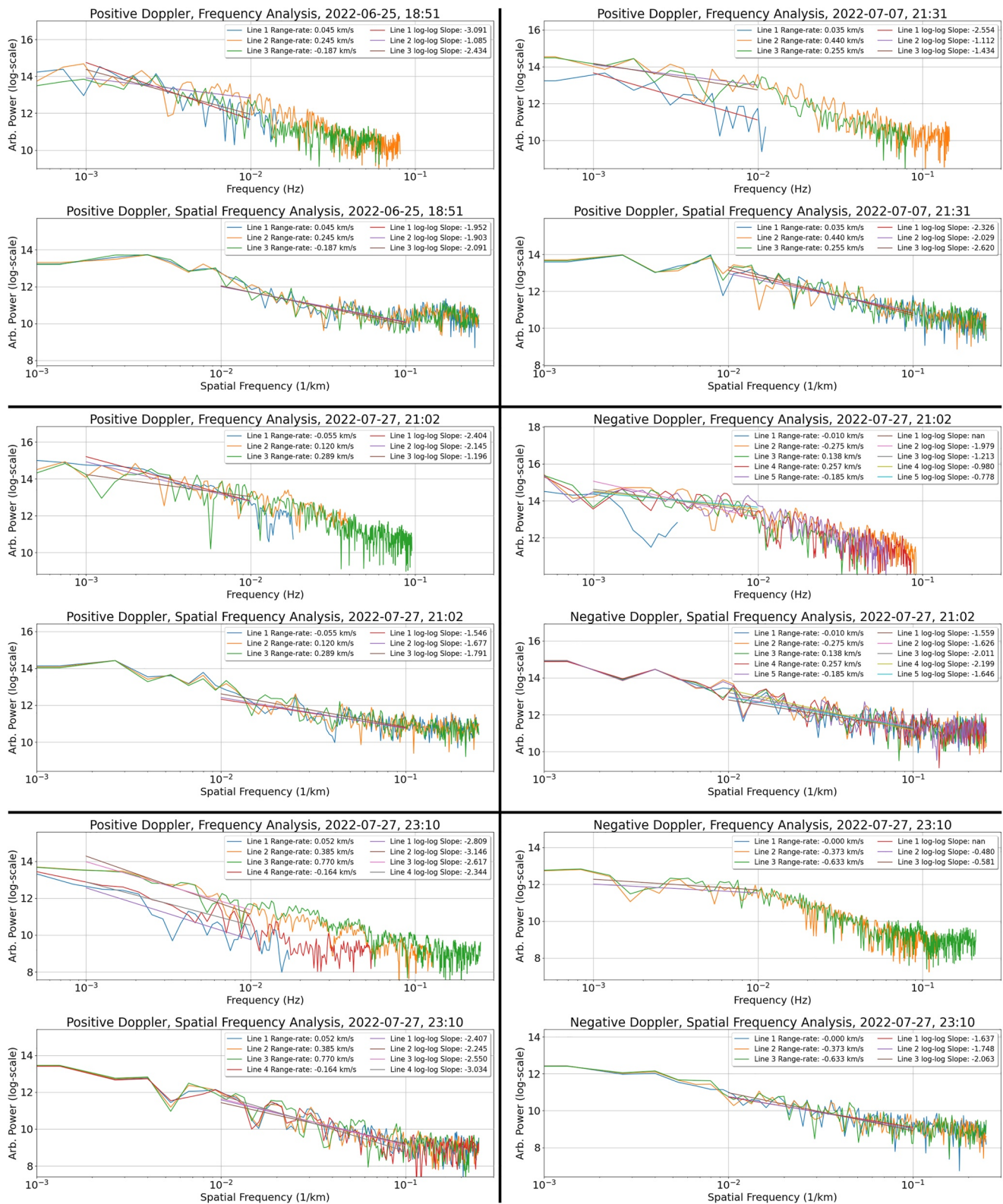
Figure 5. The spectra and slopes calculated for each of the range-rates determined from the data presented in Figure 4. Both the temporal and spatial frequencies of the data are provided, with the value of the slope between 1,000 and 100 s and 100–10 km provided in the legends.
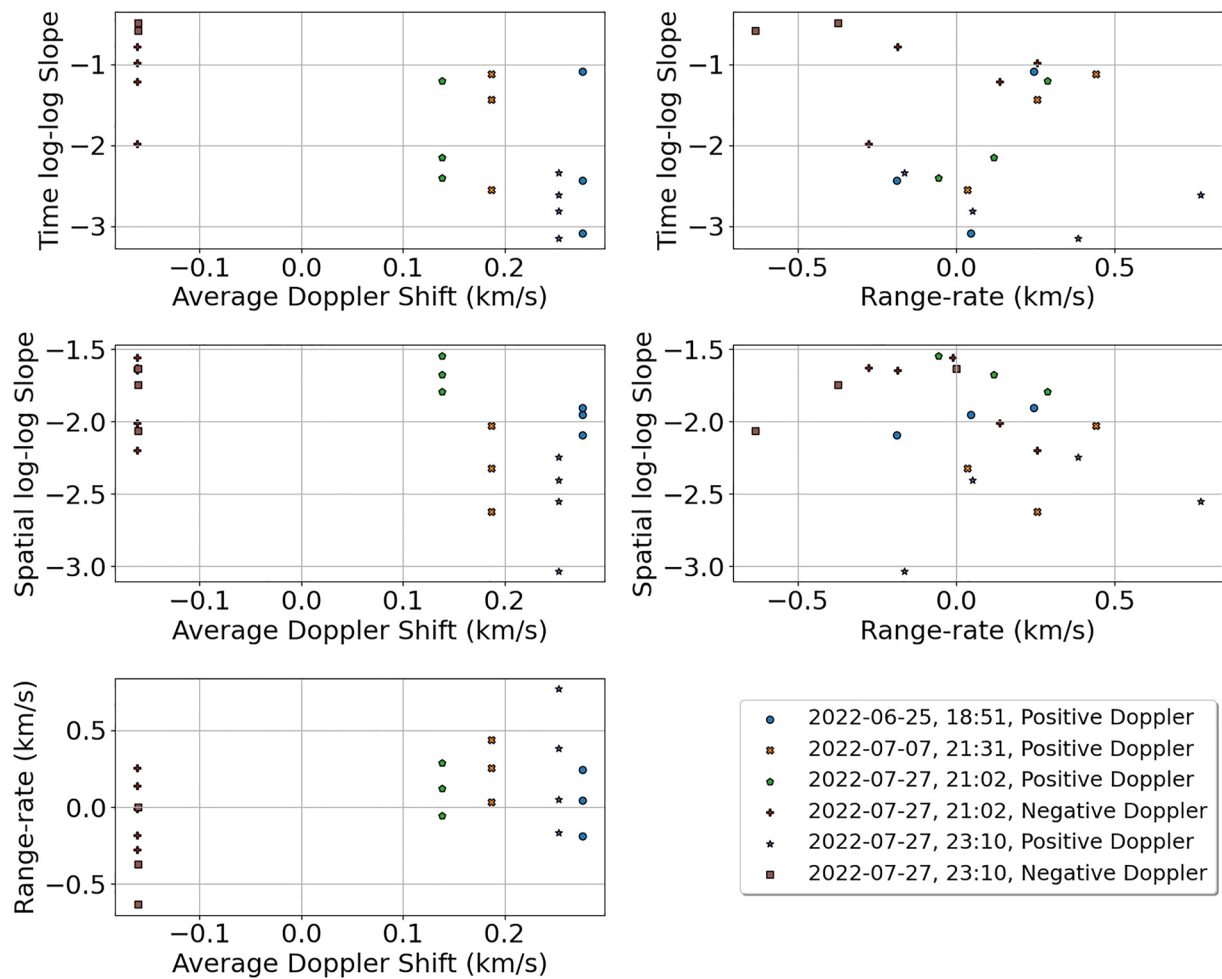
Figure 6. Summary scatter plots of the Doppler shifts and range-rates of the data plotted with the logarithmic spectral slopes in the temporal (1,000–100 s) and spatial (100–10 km) frequency domains.

To summarize Figure 6, we found the spatial frequency logarithmic spectral slopes to be in the range of −3.0 to −1.5 for scales of 100–10 km and the temporal frequency logarithmic spectral slopes were in the range of −3.5 to −0.5 for scales of 1000–100 s. We will attempt to put these results in the context of previous rocket, auroral imager, and satellite measurements of the ionosphere and the associated spectral characteristics of the ionospheric structure.

Ott and Farley (1974) showed that gradient drift instabilities in the E-region (also known as Type II irregularities) are expected to have a logarithmic spectral slope, or index, of −3.0. While the study investigated smaller scales than the large-scale ionospheric phenomena we are investigating here, it should be noted that most of our measurements in the scale size of 100–10 km had much shallower slopes than this.

If we assume a direct cascade (large scales to small scales) rather than an inverse cascade (small scales to large scales) of the energy in the spatial spectrum, we could expect that the gradient-drift or current-convective process is the cause of much of the irregularity structuring from large scale electric field fluctuations (Kintner & Seyler, 1985). With these processes, the power spectral index, or logarithmic spectral slope of the power and frequency, are expected to be −5/3. We observe a significant portion of the slopes for scales of 100–10 km between −2.0 and −1.5. The idea of an inverse cascade occurring is also intriguing, as Farley-Buneman instabilities are known to cause plasma turbulence at meter-scale sizes. From the (Kintner & Seyler, 1985) study, an inverse cascade of Kelvin-Helmholtz waves or drift waves is expected to produce electric field spectral indices of −5/3. These then provide additional mechanisms which could correspond to the E-region measurements. At least one order of magnitude improvement in range resolution would be required to further investigate the potential for

an inverse cascade, where a link between the km scales and meter scales is needed to observe the full spectrum and determine if an inverse cascade is likely.

There is also a discussion in Kintner and Seyler (1985) on electric fields measured by balloons, with a change in the spectral slopes at a scale size of ∼60 km. This change of slope is from −1.6 to −2.8 when observing smaller scale sizes. This then corresponds to a steeper slope at smaller scales. We did not see evidence of this in the structuring of the small-scale plasma turbulence at E-region altitudes. Rather, as previously discussed, there may be a change in slope around 10 km scales, where at smaller scale sizes, the slope becomes shallower. Again, there should be some caution regarding this result due to the unexpected relatively flat slope. Enhanced electric fields have been shown to accompany auroral arcs (e.g., Maynard et al., 1973), and therefore could cause the large-scale structuring of the meter-scale plasma turbulence in the E-region through instability mechanisms.

A review of ionospheric plasma turbulence by Pécseli (2015) provides an excellent summary of some of the previous work on spectral indices for the ionospheric plasma turbulence spectrum under different conditions. Electric field spectral indices are listed between −4.5 and −1 from measurements at multiple different altitudes from satellites and rockets. There is also one spectral index slope of −1 listed for E-region plasma density measured by rockets, while the rest of the density measurements are for the F-region and therefore not considered here. We expect the electric field fluctuations are relatively consistent along a magnetic field line, at least for scales greater than 1 km, which is why these spectral indices from previous studies are mentioned. A goal of the spectral index research is to determine the structuring of instability and turbulence sources from the spectral slopes and observe how energy is distributed across the scales to compare with turbulence theory. Due to the range of previously measured spectral index values and differences in measurement methods, this can be a difficult endeavor. For now, we consider the spectral indices measured in the current study to be similar to the values and spread of spectral indices measured by previous researchers. This then highlights the viability of using E-region coherent scatter for investigation of lower ionospheric turbulence structuring.

This study also shows that observing plasma structuring in the reference frame of different bulk plasma velocities does result in differences in the slopes determined. This is a factor that should be considered when determining the structure of ionospheric irregularities and instability sources, especially on large spatial scales. The bulk of the small-scale E-region plasma turbulence structuring does occur at small range-rates, meaning that over relatively long periods of time the greater than km scale turbulence sources corresponding to ionospheric electric fields and plasma densities changed locations slowly.

4. Summary

We have highlighted the capability of the SIMONe Norway meteor radar system to measure the spectral characteristics of large-scale ionospheric and magnetospheric phenomena through the use of small-scale plasma density turbulence as a tracer. The large-scale phenomena will structure the ionospheric plasma densities and electric fields which generate the small-scale plasma density turbulence. The plasma density turbulence can be scattered by using coherent scatter radar techniques.

The range-rates of the large-scale structures were determined by using 2D Fourier analysis techniques on the range-time-intensity coherent scatter data. The bulk of the structuring in the E-region for the dates investigated is found to have range-rates of approximately 0 km/s. This corresponds to most of the large-scale sources driving the small-scale (∼5 m for SIMONe) plasma turbulence being relatively slow-moving on macroscopic scales. Investigating sub-km scales requires finer resolutions than those provided from the analysis here, or requires a multi-frequency radar setup. The determined range-rates of the large-scale ionospheric structuring were used to examine the spatial and temporal structuring of the ionosphere in the reference frame of the bulk plasma motion.

The spatial frequency analysis on scales of 100–10 km had logarithmic spectral slopes of −3 to −1.5. This agrees with much of the previous work on the spatial spectra scaling for ionospheric electric fields (e.g., Kintner & Seyler, 1985; Pécseli, 2015). Electric fields are the source for much of the auroral E-region plasma turbulence, so it is expected that the data should have similar structuring at large scales for both F-region and E-region measurements. Interestingly enough, at scales smaller than 10 km, the spatial spectra measurements presented here showed a flattening in the slope, and sometimes even a positive slope. This result should be considered cautiously as the spectral slopes are unexpectedly relatively flat and do approach the Nyquist sampling limit of 3 km. None-

theless, turbulence with 10 km scale sizes could correspond to the scale sizes of auroral arcs and field-aligned currents (e.g., Ivarsen, Lozinsky, et al., 2023; Samson et al., 1996). Also, a recent study by Billett et al. (2022) analyzed the Poynting flux into ionosphere, and found that a significant proportion of the energy budget comes from small-scale variability. We leave further investigation into the flattening of the spectra and the structuring at these scales to future work using finer-resolution experiments.

The temporal logarithmic spectral slopes were also investigated on scales of 1,000–100 s and values of -3.2 to -0.5 were determined. The temporal power spectra correspond to the change in the structuring of the turbulence over time. At scales of 100–10 s, there appears to commonly be a steepening of the spectral slopes. This would mean that at relatively longer time scales (>300 s), the magnetosphere injects power into the E-region. That stated, the trends in the temporal power spectra are less clear and more data are required before drawing any conclusions. The Nyquist limits of the temporal spectral analysis were ~ 4 s due to the 2 s averaging of the coherent scatter measurements.

In summary, it is clear that SIMONe systems can be used to monitor both the neutral and charged components of atmospheric structuring and turbulence at mesosphere and lower ionosphere altitudes, with neutral atmospheric structuring over northern Germany using SIMONe being recently shown by Poblet et al. (2023). The analysis presented in the current study could be also implemented on other radars, such as the ones shown in the studies of Hysell et al. (2012), Chau and St.-Maurice (2016), Bristow (2019), Lozinsky et al. (2022), and McWilliams et al. (2023). Future E-region studies with SIMONe will utilize larger data sets and the multi-static radar links to further investigate ionospheric plasma turbulence and links between the neutral and charged atmospheric processes over the northern Fennoscandian sector.

Data Availability Statement

The DOI for the SIMONe radar data used to create the figures in this publication can be found in the references (Huyghebaert, 2023).

References

Archer, M. O., Hartinger, M. D., Rastätter, L., Southwood, D. J., Heyns, M., Eggington, J. W. B., et al. (2023). Auroral, ionospheric and ground magnetic signatures of magnetopause surface modes. *Journal of Geophysical Research: Space Physics*, *128*(3), e2022JA031081. https://doi.org/10.1029/2022JA031081

Billett, D. D., McWilliams, K. A., Pakhotin, I. P., Burchill, J. K., Knudsen, D. J., & Martin, C. J. (2022). High-resolution Poynting flux statistics from the Swarm mission: How much is being underestimated at larger scales? *Journal of Geophysical Research: Space Physics*, *127*(7), e2022JA030573. https://doi.org/10.1029/2022JA030573

Bristow, W. A. (2019). Application of radar imaging analysis to superdarn observations. *Radio Science*, *54*(7), 692–703. https://doi.org/10.1029/2019RS006851

Buneman, O. (1963). Excitation of field aligned sound waves by electron streams. *Physical Review Letters*, *10*(7), 285–287. https://doi.org/10.1103/PhysRevLett.10.285

Chaston, C. C., Seki, K., Sakanoi, T., Asamura, K., Hirahara, M., & Carlson, C. W. (2011). Cross-scale coupling in the auroral acceleration region. *Geophysical Research Letters*, *38*(20), L20101. https://doi.org/10.1029/2011GL049185

Chau, J. L., & St.-Maurice, J.-P. (2016). Unusual 5 m E region field-aligned irregularities observed from northern Germany during the magnetic storm of 17 March 2015. *Journal of Geophysical Research: Space Physics*, *121*(10), 10316–10340. https://doi.org/10.1002/2016JA023104

Chau, J. L., Urco, J. M., Vierinen, J., Harding, B. J., Clahsen, M., Pfeffer, N., et al. (2021). Multistatic specular meteor radar network in Peru: System description and initial results. *Earth and Space Science*, *8*(1), e2020EA001293. https://doi.org/10.1029/2020EA001293

Chau, J. L., Urco, J. M., Vierinen, J. P., Volz, R. A., Clahsen, M., Pfeffer, N., & Trautner, J. (2019). Novel specular meteor radar systems using coherent MIMO techniques to study the mesosphere and lower thermosphere. *Atmospheric Measurement Techniques*, *12*(4), 2113–2127. https://doi.org/10.5194/amt-12-2113-2019

Debue, P., Kuzzay, D., Saw, E.-W., Daviaud, F., Dubrulle, B., Canet, L., et al. (2018). Experimental test of the crossover between the inertial and the dissipative range in a turbulent swirling flow. *Physical Review Fluids*, *3*(2), 024602. https://doi.org/10.1103/PhysRevFluids.3.024602

Farley, D. T. (1963). A plasma instability resulting in field-aligned irregularities in the ionosphere. *Journal of Geophysical Research*, *68*(22), 6083–6097. https://doi.org/10.1029/JZ068i022p06083

Fejer, B. G., & Kelley, M. C. (1980). Ionospheric irregularities. *Reviews of Geophysics*, *18*(2), 401–454. https://doi.org/10.1029/RG018i002p00401

Gillies, R. G., Hussey, G. C., Sofko, G. J., McWilliams, K. A., Fiori, R. A. D., Ponomarenko, P., & St.-Maurice, J.-P. (2009). Improvement of SuperDARN velocity measurements by estimating the index of refraction in the scattering region using interferometry. *Journal of Geophysical Research: Space Physics*, *114*(A7), A07305. https://doi.org/10.1029/2008JA013967

Huyghebaert, D. (2023). *HuyghebaertJGR2023*. Leibniz Institute of Atmospheric Physics at the University of Rostock. https://doi.org/10.22000/990

Huyghebaert, D., Clahsen, M., Chau, J. L., Renkwitz, T., Latteck, R., Johnsen, M. G., & Vierinen, J. (2022). Multiple E-Region radar propagation modes measured by the VHF SIMONe Norway system during active ionospheric conditions. *Frontiers in Astronomy and Space Sciences*, *9*, 886037. https://doi.org/10.3389/fspas.2022.886037

Huyghebaert, D., Hussey, G., Vierinen, J., McWilliams, K., & St-Maurice, J.-P. (2019). ICEBEAR: An all-digital bistatic coded continuous-wave radar for studies of the E region of the ionosphere. *Radio Science*, *54*(4), 349–364. https://doi.org/10.1029/2018RS006747

Huyghebaert, D., St.-Maurice, J.-P., McWilliams, K., Hussey, G., Howarth, A. D., Rutledge, P., & Erion, S. (2021). The properties of ICEBEAR E-region coherent radar echoes in the presence of near infrared auroral emissions, as measured by the Swarm-E Fast Auroral Imager. *Journal of Geophysical Research: Space Physics*, *126*(12), e2021JA029857. https://doi.org/10.1029/2021JA029857

Hysell, D. (2015). The radar aurora. In *Auroral dynamics and space weather* (pp. 191–209). American Geophysical Union. https://doi.org/10.1002/9781118978719.ch14

Hysell, D., & Larsen, M. F. (2021). VHF imaging radar observations and theory of banded midlatitude sporadic E ionization layers. *Journal of Geophysical Research: Space Physics*, *126*(5), e2021JA029257. https://doi.org/10.1029/2021JA029257

Hysell, D., Miceli, R., Munk, J., Hampton, D., Heinselman, C., Nicolls, M., et al. (2012). Comparing VHF coherent scatter from the radar aurora with incoherent scatter and all-sky auroral imagery. *Journal of Geophysical Research: Space Physics*, *117*(A10), A10313. https://doi.org/10.1029/2012JA018010

Ivarsen, M. F., Jin, Y., Spicher, A., & Clausen, L. B. N. (2019). Direct evidence for the dissipation of small-scale ionospheric plasma structures by a conductive E region. *Journal of Geophysical Research: Space Physics*, *124*(4), 2935–2942. https://doi.org/10.1029/2019JA026500

Ivarsen, M. F., Lozinsky, A., St-Maurice, J.-P., Spicher, A., Huyghebaert, D., Hussey, G. C., et al. (2023). The distribution of small-scale irregularities in the E-region, and its tendency to match the spectrum of field-aligned current structures in the F-region. *Journal of Geophysical Research: Space Physics*, *128*(5), e2022JA031233. https://doi.org/10.1029/2022JA031233

Ivarsen, M. F., St-Maurice, J.-P., Hussey, G. C., Galeschuk, D., Lozinsky, A., Pitzel, B., & McWilliams, K. A. (2023). An algorithm to separate ionospheric turbulence radar echoes from those of meteor trails in large data sets. *Journal of Geophysical Research: Space Physics*, *128*(1). e2022JA031050. https://doi.org/10.1029/2022JA031050

Ivarsen, M. F., St-Maurice, J.-P., Jin, Y., Park, J., Miloch, W., Spicher, A., et al. (2021). Steepening plasma density spectra in the ionosphere: The crucial role played by a strong E-region. *Journal of Geophysical Research: Space Physics*, *126*(8), e2021JA029401. https://doi.org/10.1029/2021JA029401

Kintner, P. M., & Seyler, C. E. (1985). The status of observations and theory of high latitude ionospheric and magnetospheric plasma turbulence. *Space Science Reviews*, *41*(1–2), 91–129. https://doi.org/10.1007/BF00241347

Kivanç, Ö., & Heelis, R. A. (1998). Spatial distribution of ionospheric plasma and field structures in the high-latitude F region. *Journal of Geophysical Research: Space Physics*, *103*(A4), 6955–6968. https://doi.org/10.1029/97JA03237

Kolmogorov, A. N., Levin, V., Hunt, J. C. R., Phillips, O. M., & Williams, D. (1991). The local structure of turbulence in incompressible viscous fluid for very large Reynolds numbers. *Proceedings of the Royal Society of London. Series A: Mathematical and Physical Sciences*, *434*(1890), 9–13. https://doi.org/10.1098/rspa.1991.0075

Kozelov, B. V., & Rypdal, K. (2007). Spatial scaling of optical fluctuations during substorm-time aurora. *Annales Geophysicae*, *25*(4), 915–927. https://doi.org/10.5194/angeo-25-915-2007

Lozinsky, A., Hussey, G., McWilliams, K., Huyghebaert, D., & Galeschuk, D. (2022). ICEBEAR-3D: A low elevation imaging radar using a non-uniform coplanar receiver array for E region observations. *Radio Science*, *57*(3), e2021RS007358. https://doi.org/10.1029/2021RS007358

Maynard, N. C., Bahnsen, A., Christophersen, P., Egeland, A., & Lundin, R. (1973). An example of anticorrelation of auroral particles and electric fields. *Journal of Geophysical Research*, *78*(19), 3976–3980. https://doi.org/10.1029/JA078i019p03976

McWilliams, K. A., Detwiller, M., Kotyk, K., Krieger, K., Rohel, R., Billett, D. D., et al. (2023). Borealis: An advanced digital hardware and software design for SuperDARN radar systems. *Radio Science*, *58*(3), e2022RS007591. https://doi.org/10.1029/2022RS007591

Nakai, H., Kamide, Y., Hardy, D. A., & Gussenhoven, M. S. (1986). Time scales of expansion and contraction of the auroral oval. *Journal of Geophysical Research*, *91*(A4), 4437–4450. https://doi.org/10.1029/JA091iA04p04437

Ott, E., & Farley, D. T. (1974). The k spectrum of ionospheric irregularities. *Journal of Geophysical Research*, *79*(16), 2469–2472. https://doi.org/10.1029/JA079i016p02469

Pakhotin, I. P., Mann, I. R., Lysak, R. L., Knudsen, D. J., Gjerloev, J. W., Rae, I. J., et al. (2018). Diagnosing the role of Alfvén waves in magnetosphere-ionosphere coupling: Swarm observations of large amplitude nonstationary magnetic perturbations during an interval of northward IMF. *Journal of Geophysical Research: Space Physics*, *123*(1), 326–340. https://doi.org/10.1002/2017JA024713

Pécseli, H. L. (2015). Spectral properties of electrostatic drift wave turbulence in the laboratory and the ionosphere. *Annales Geophysicae*, *33*(7), 875–900. https://doi.org/10.5194/angeo-33-875-2015

Poblet, F. L., Vierinen, J., Avsarkisov, V., Conte, J. F., Charuvil Asokan, H., Jacobi, C., & Chau, J. L. (2023). Horizontal correlation functions of wind fluctuations in the mesosphere and lower thermosphere. *Journal of Geophysical Research: Atmospheres*, *128*(6), e2022JD038092. https://doi.org/10.1029/2022JD038092

Samson, J. C., Cogger, L. L., & Pao, Q. (1996). Observations of field line resonances, auroral arcs, and auroral vortex structures. *Journal of Geophysical Research: Space Physics*, *101*(A8), 17373–17383. https://doi.org/10.1029/96JA01086

Shi, X., Ruohoniemi, J. M., Baker, J. B. H., Lin, D., Bland, E. C., Hartinger, M. D., & Scales, W. A. (2018). Survey of ionospheric Pc3-5 ULF wave signatures in SuperDARN high time resolution data. *Journal of Geophysical Research: Space Physics*, *123*(5), 4215–4231. https://doi.org/10.1029/2017JA025033

Spicher, A., Miloch, W. J., & Moen, J. I. (2014). Direct evidence of double-slope power spectra in the high-latitude ionospheric plasma. *Geophysical Research Letters*, *41*(5), 1406–1412. https://doi.org/10.1002/2014GL059214

St.-Maurice, J.-P., & Chau, J. L. (2016). A theoretical framework for the changing spectral properties of meter-scale Farley-Buneman waves between 90 and 125 km altitudes. *Journal of Geophysical Research: Space Physics*, *121*(10), 10341–10366. https://doi.org/10.1002/2016JA023105

St.-Maurice, J. P., Prikryl, P., Danskin, D. W., Hamza, A. M., Sofko, G. J., Koehler, J. A., et al. (1994). On the origin of narrow non-ion-acoustic coherent radar spectra in the high-latitude E region. *Journal of Geophysical Research*, *99*(A4), 6447–6474. https://doi.org/10.1029/93JA02353

Vierinen, J., Chau, J. L., Charuvil, H., Urco, J. M., Clahsen, M., Avsarkisov, V., et al. (2019). Observing mesospheric turbulence with specular meteor radars: A novel method for estimating second-order statistics of wind velocity. *Earth and Space Science*, *6*(7), 1171–1195. https://doi.org/10.1029/2019EA000570